Laramide Deformation and Flexural Effects in the Upper Cretaceous: A Basin in Transition*

Kurt W. Rudolph[1] and Joel P. Saylor[1]

Search and Discovery Article #30578 (2018)**
Posted September 24, 2018

*Adapted from extended abstract prepared for oral presentation given at 2018 AAPG Annual Convention & Exhibition, Salt Lake City, Utah, May 20-23, 2018.
 DOI:10.1306/30578Rudolph2018

[1]University of Houston, Houston, TX (kwrudolph@comcast.net)

Abstract

The nature of subsidence in the Western Interior evolved in the Late Cretaceous from a contiguous (Sevier) foreland to partitioned (Laramide) basins coeval with an increase in long-wavelength “dynamic” subsidence (Yonkee and Weil, 2015). This evolution is interpreted by many (e.g., Painter and Carrapa, 2013; Liu et al., 2014) as indicators of flat-slab subduction. However, the timing and geographic location of changing subsidence mechanisms remains poorly documented. To better assess the geodynamic mechanisms responsible for this transition, we have mapped active elements versus time, including classic retroarc foredeeps, intra-basinal uplifts, long-wavelength subsidence, and local flexural wedges adjacent to rising Laramide structures. Criteria include isopachs, paleogeography, geohistory analysis, unconformities/exhumation, and sediment-dispersal patterns.

Analysis

The analysis identified a continuous foredeep adjacent to the Sevier fold-thrust belt through the Santonian, but not subsequently. Long-wavelength “dynamic” subsidence in the basin commences in the Coniacian and Santonian, but is less important subsequently. As evidenced by isopach patterns, Laramide structures first began growing in the Cenomanian–Turonian. The influence of Laramide uplifts increased over time, as flexure associated with these uplifts became a dominant subsidence mechanism by the Maastrichtian.

Sixteen flexural stratigraphic wedges (Figures 1 and 2), associated with both Sevier and Laramide uplifts, have been used to quantitatively model loads and the effective elastic thicknesses (EET) of the coupled lithosphere. The forward modeling algorithm varies key parameters over a range, using a Monte Carlo simulation. Models whose flexed profiles pass within uncertainty of the observed stratigraphic thickness at up to five control points over the observed 2-D profile are retained (Figure 3). These are used to calculate the mean and standard deviation of load height, load width, load density, and EET. At least 50,000 trials are run, with usually just a few percent passing the error criterion. This approach has the advantage of removing interpretation bias, as a large range of model parameters are tested.

Results

Results indicate that EET decreases from the late Cenomanian–Turonian to the late Campanian–Maastrichtian in the western portions of the area (Figures 4 and 5). Because EET is a measure of the integrated strength of the lithosphere, the modeled decrease may be a factor in enabling Laramide deformation and the associated basin partitioning. The decrease in effective elastic thickness of the lithosphere is consistent with lithospheric weakening induced by the introduction of volatiles during flat-slab subduction.

We observe a close correlation between modeled EET in the late Campanian–Maastrichtian and modern estimates of EET from joint inversion of gravity data and seismic tomography (Figures 6 and 7; Tesauro et al., 2015). This supports the hypothesis that flat-slab subduction preconditioned the lithosphere for subsequent Cenozoic tectonic and magmatic events.

Large-scale petroleum system play elements are correlated with the distribution of these tectonic elements and associated subsidence. Examples include the Lance Formation fluvial reservoir at the Pinedale Field and the Lewis Formation source/seal and submarine fans in the Washakie Basin. Both are associated with thick stratigraphy deposited in Maastrichtian flexural basins that developed adjacent to the Wind River and Granite mountains, respectively. Another instance is the Niobrara source/”shale oil” reservoir in the Sand Wash, eastern Piceance, and Denver basins, which is associated with the onset of rapid dynamic subsidencethat effectively starved the basins of coarse clastic detritus.

References Cited

Liu, S., D. Nummedal, and M. Gurnis, 2014, Dynamic versus flexural controls of Late Cretaceous Western Interior Basin, USA: Earth and Planetary Science Letters, v. 389, p. 221-229, doi: http://dx.doi.org/10.1016/j.epsl.2014.01.006.

Painter, C.S., and B. Carrapa, 2013, Flexural versus dynamic processes of subsidence in the North American Cordillera foreland basin: Geophysical Research Letters, v. 40, p. 4249–4253, doi: 10.1002/grl.50831, 2013.

Saylor, J.E., J.C. Jordan, K.E. Sundell, X. Wang, S. Wang, and T. Deng, 2017, Topographic growth of the Jishi Shan and its impact on basin and hydrology evolution, NE Tibetan Plateau: Basin Research, doi: 10.1111/bre.12264.

Tesauro, M., M.K. Kaban, and W.D. Mooney, 2015, Variations of the lithospheric strength and elastic thickness in North America: Geochemistry, Geophysics, Geosystems, v. 16, p. 2197-2220, doi: 10.1002/2015GC005937.

Yonkee, W.A., and A.B. Weil, 2015, Tectonic evolution of the Sevier and Laramide belts within the North American Cordillera orogenic system: Earth-Science Reviews, v. 150, p. 531-593, dx.doi.org/10.1016/j.earscirev.2015.08.001.

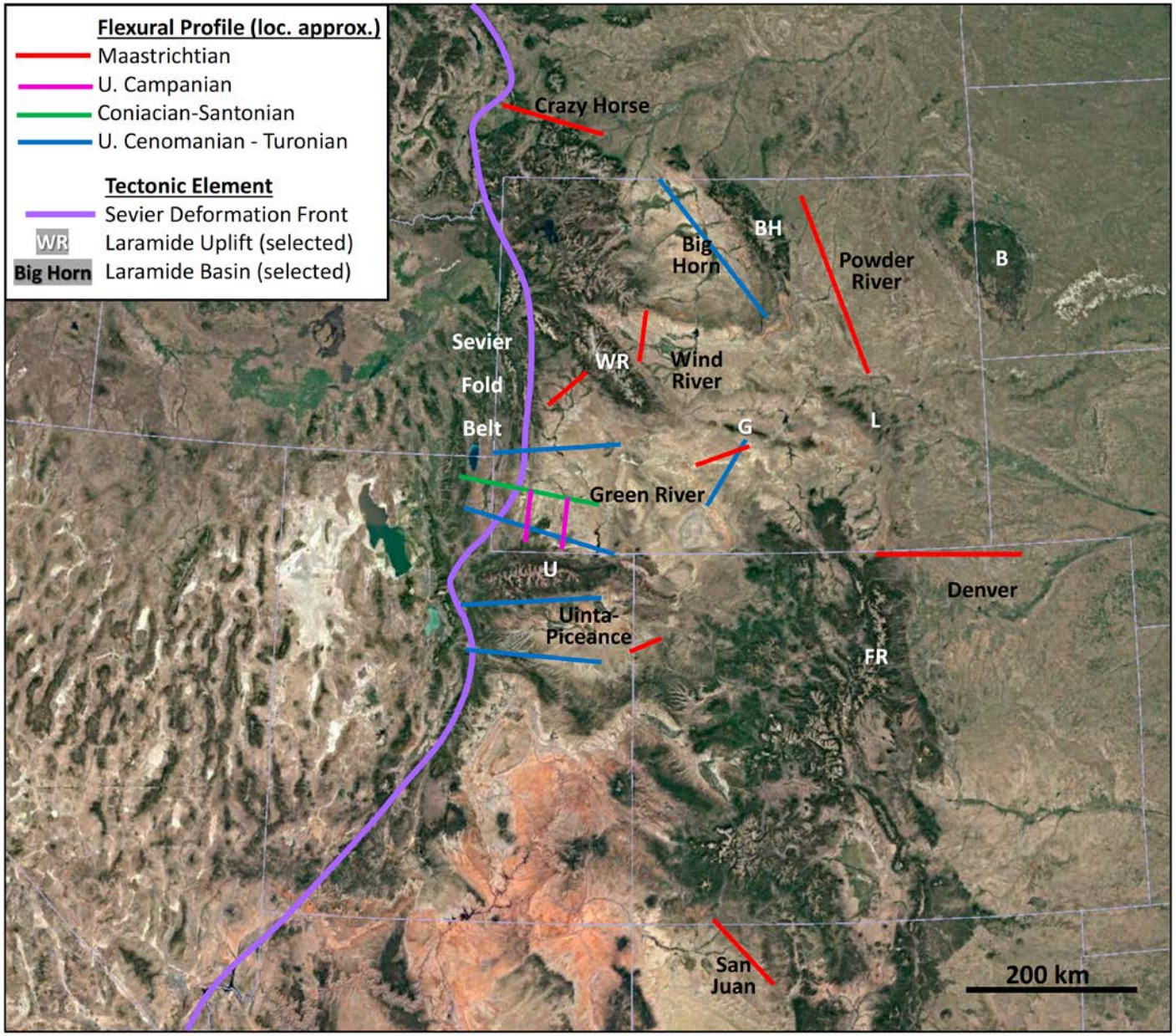

Figure 1. Location map showing the flexural profiles and selected flexural loads. Abbreviations: B: Black Hills, BH: Bighorn Mountains, FR: Front Range, G: Granite Mountains, L: Laramie Mountains, U: Uinta Mountains, WR: Wind River Range

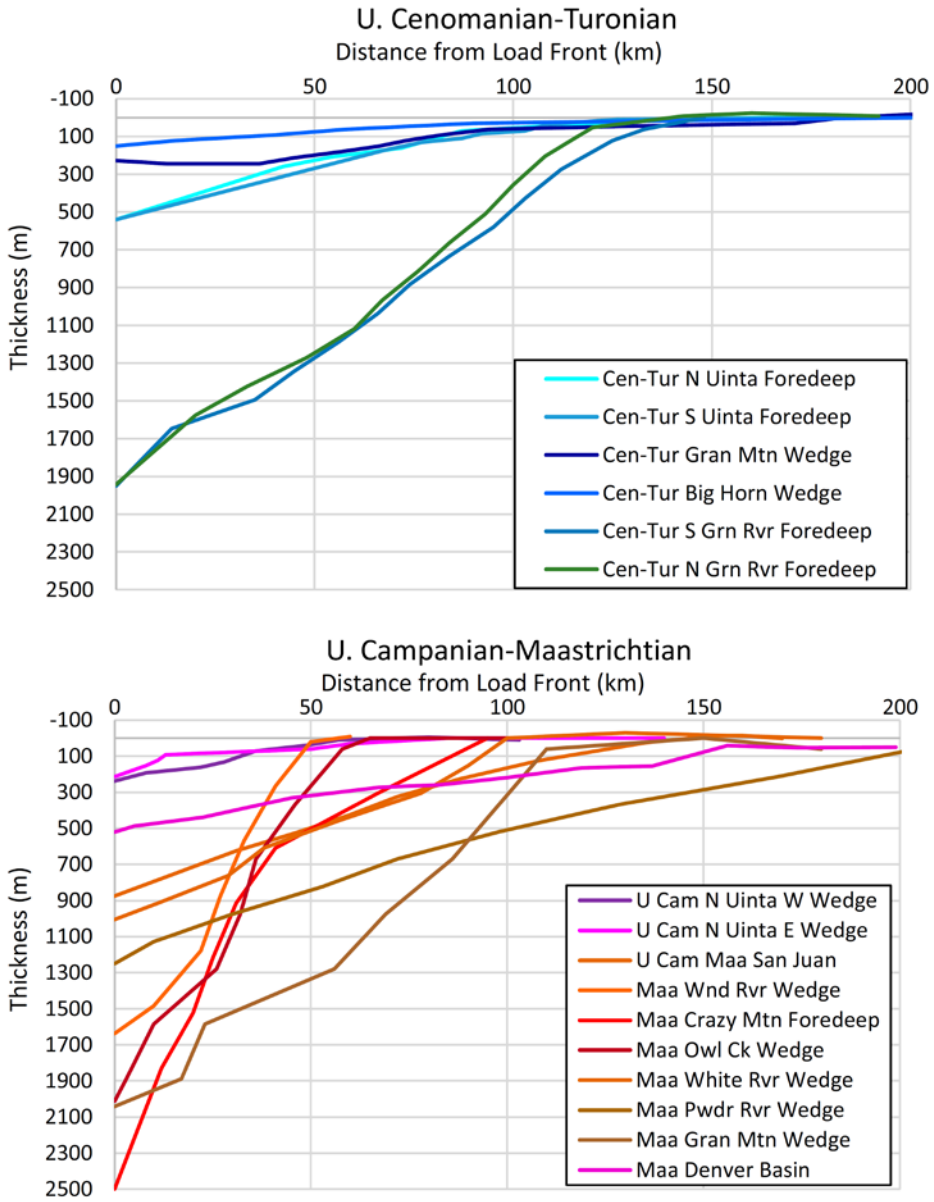

Figure 2. Upper Cenomanian–Turonian (top) and upper Campanian–Maastrichtian (bottom) flexural profiles built from well and outcrop control. The older profiles are relatively long wavelength, whereas the younger profiles are quite variable; narrower wedges are generally in the west.

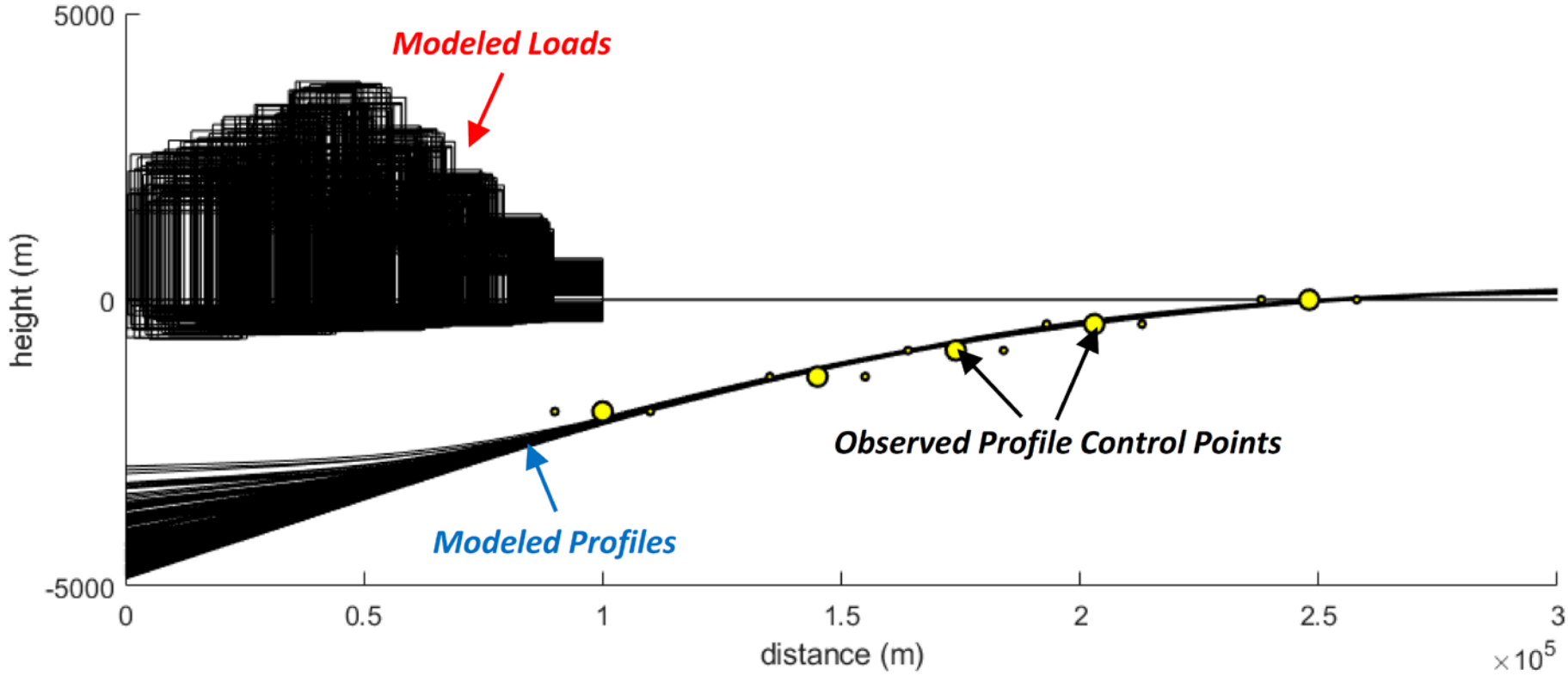

Figure 3. Example of a flexural model using a Monte Carlo simulation approach. This case is for the upper Cenomanian–Turonian foreland wedge (approximately the equivalent of the Frontier Formation interval) in the southern Green River Basin. The example has been modeled assuming a broken plate and load blocks whose height taper to the right. Each curve and load profile is a trial that passed the uncertainty window (small yellow circles) around the observed control points (large yellow circles). About 0.2% of 100,000 trials were admissible. See Saylor et al. (2017) for a complete description of the model approach and parameters.

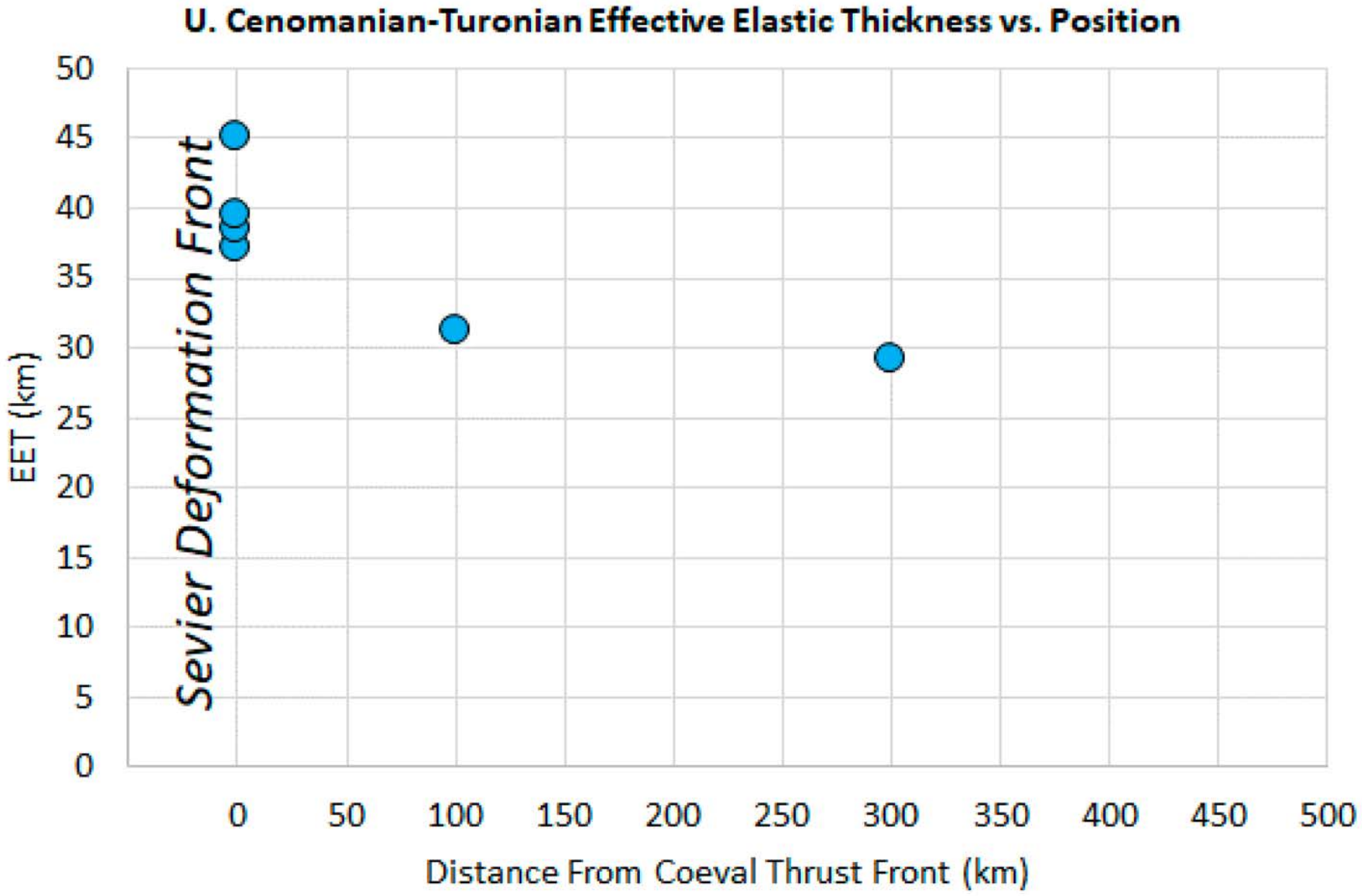

Figure 4. Estimates of effective elastic thickness (EET) for the upper Cenomanian–Turonian interval plotted against distance from the restored coeval Sevier deformation front. The EET estimates are from flexural modeling and are consistently high (≥30 km). Standard deviation for each point ranges from 0.8 to 5.5 km.

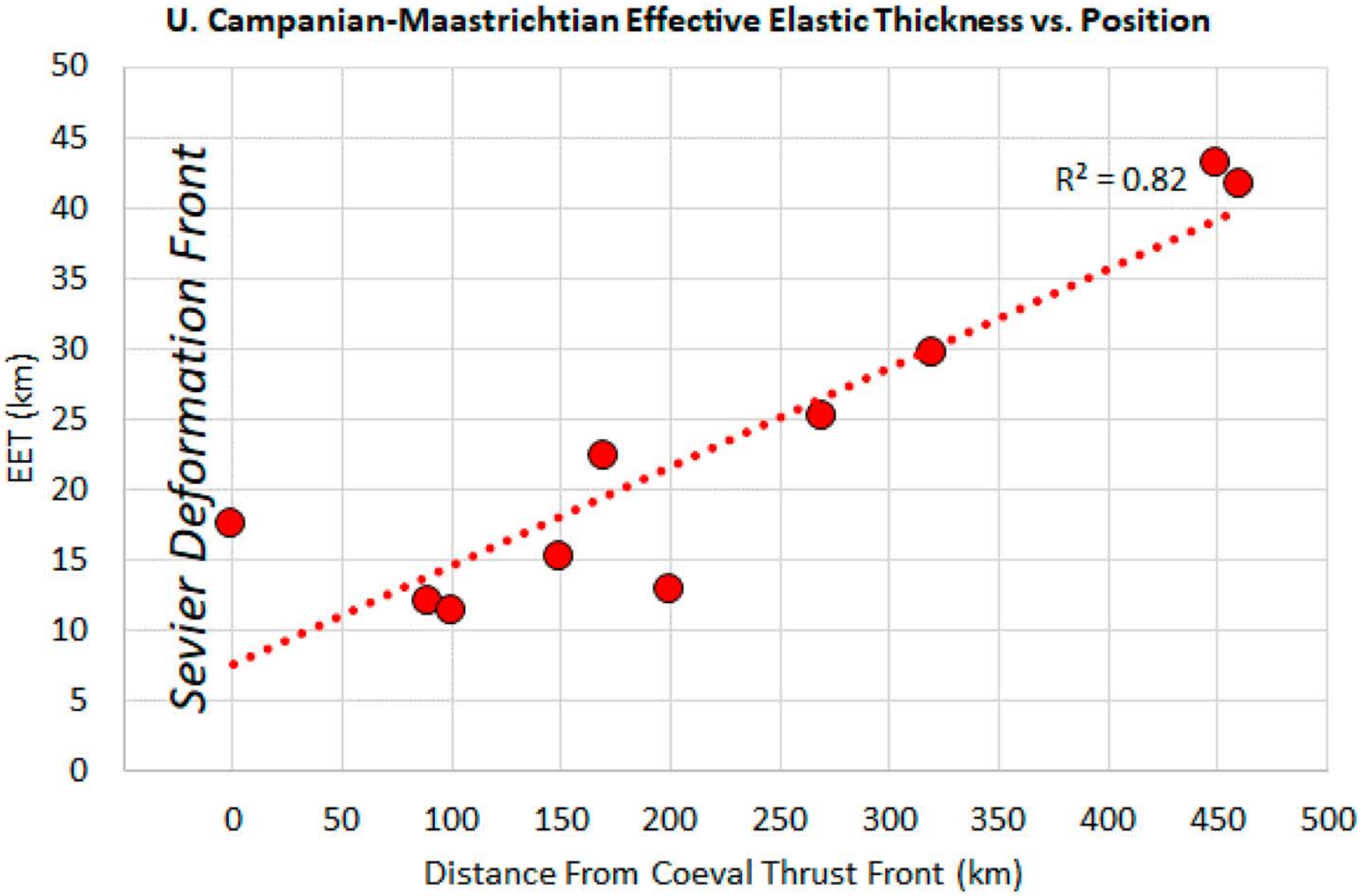

Figure 5. Estimates of effective elastic thickness (EET) for the upper Campanian–Maastrichtian interval plotted against distance from the restored coeval Sevier deformation front. EET estimates are relatively low in the western sites (<25 km) but remain high to the east (>25 km). Standard deviation for each point ranges from 0.9 to 3.7 km.

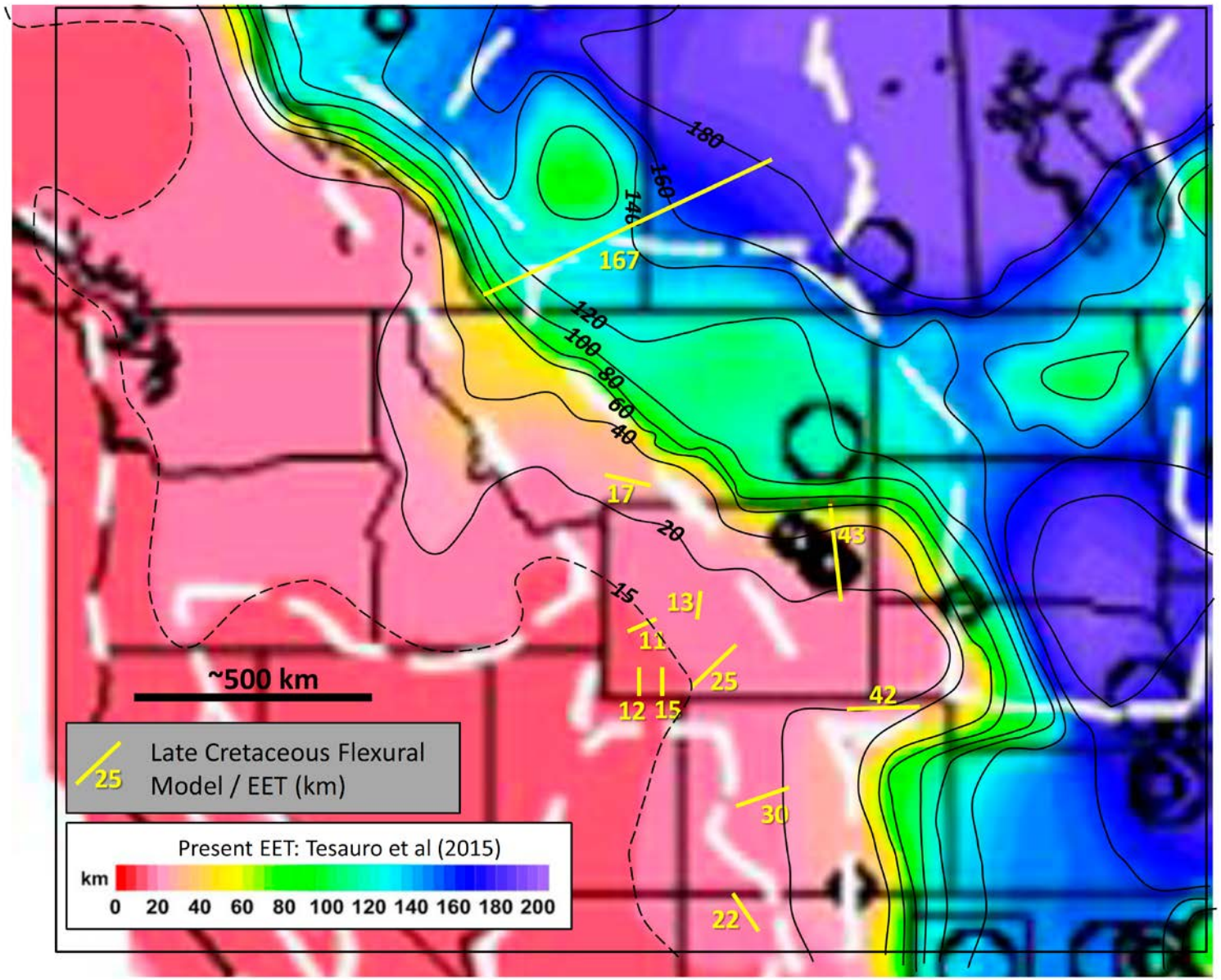

Figure 6. Present effective elastic thickness (EET, from Tesuaro et al. 2015, their Figure 8a) overlaid with the upper Campanian to Maastrichtian flexural profiles and EET estimates from this study (yellow lines). There is a general correspondence between the present-day and uppermost Cretaceous estimates.

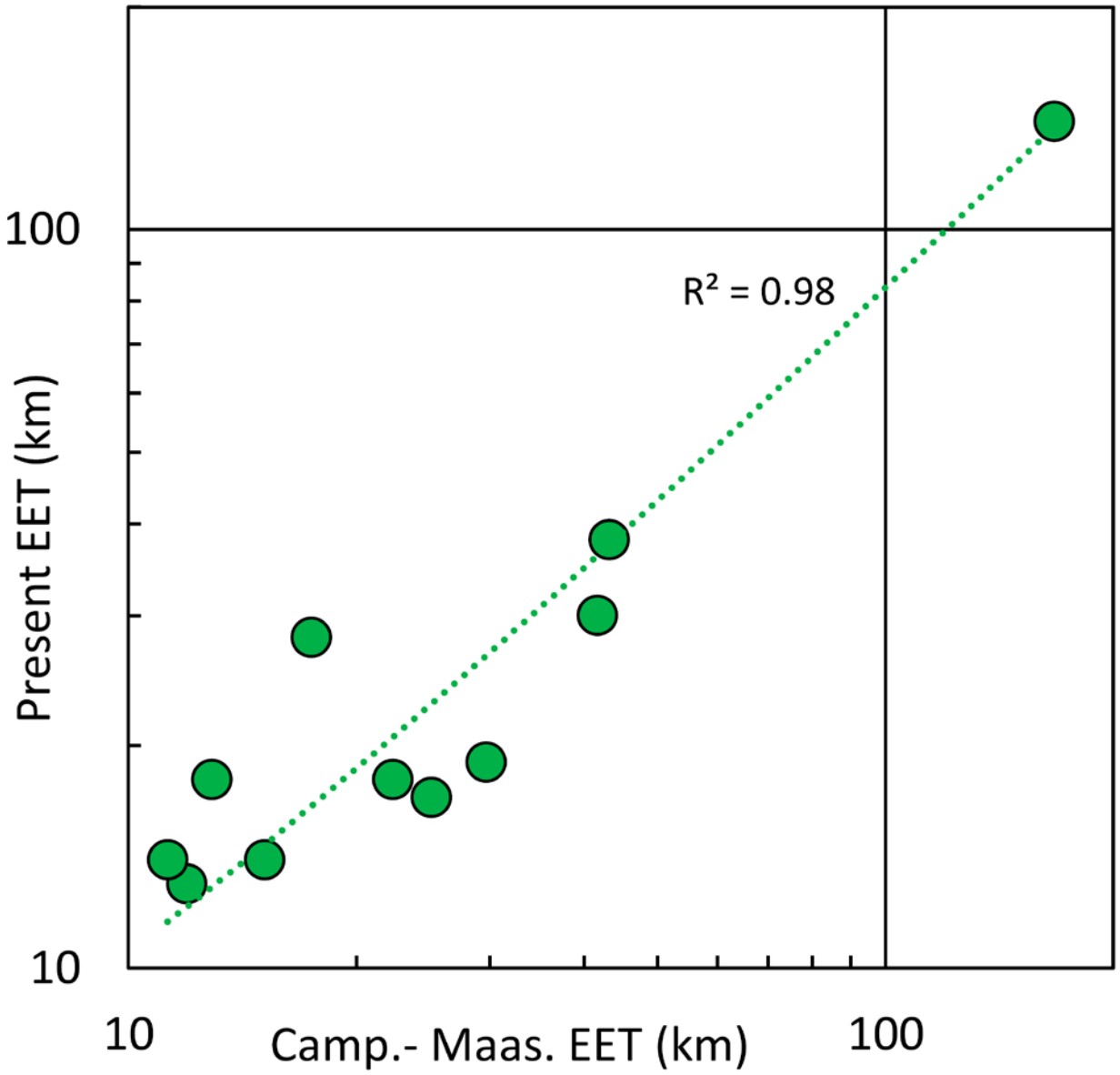

Figure 7. Estimates of modern versus upper Campanian–Maastrichtian effective elastic thickness plotted on log-log axes. The current estimates are derived from Tesauro et al. (2015) by roughly averaging over the superimposed flexural profile (see Figure 6). The Cretaceous estimates are from those flexural models (this study).